ARTICLES SCIENCE CHINA Materials

mater.scichina.com link.springer.com

Published online 16 March 2017 | doi: 10.1007/s40843-017-9017-6
Sci China Mater 2017, 60(4): 324–334

In situ electrochemically converting Fe_2O_3-$Ni(OH)_2$ to $NiFe_2O_4$-NiOOH: a highly efficient electrocatalyst towards water oxidation

Fang Zhang[1†], Yanmei Shi[1†], Tao Xue[2], Jingfang Zhang[1], Yu Liang[1] and Bin Zhang[1*]

ABSTRACT To develop low-cost, earth-abundant NiFe-based materials as highly efficient oxygen evolution reaction (OER) electrocatalysts and to probe new catalytic species are still great challenges to now. Here, an *in situ* formation of OER active $NiFe_2O_4$-NiOOH nanosheet arrays is demonstrated as a highly efficient OER electrocatalyst by the anodization of Fe_2O_3 domains anchored on $Ni(OH)_2$ nanosheet arrays. The as-converted product can deliver the current density of 30 mA cm^{-2} with a small overpotential of 240 mV, and only requires an overpotential of 410 mV to achieve an amazing huge current density of 3000 mA cm^{-2}. *In situ* potential-dependent Raman spectroscopy reveals that $Ni(OH)_2$ in the composite is easier to be oxidized to NiOOH than pure $Ni(OH)_2$, and the newly formed NiOOH reacts with the nearby Fe_2O_3 to produce hybrid $NiFe_2O_4$-NiOOH. It is found that the cooperative effect of the *in situ* formed $NiFe_2O_4$ and NiOOH as well as the hydrophilic and aerophobic electrode surface make main contribution to the outstanding OER activity of the catalyst. This work will bring new perspectives to the recognition of the origin of NiFe composite materials for OER and provide a mild method to synthesize amorphous spinel materials at room temperature.

Keywords: chemical transformation, electrocatalysis, Raman spectroscopy, oxygen evolution reaction, nanosheet array

INTRODUCTION

Sharp consuming of fossil energy and the undesirable consequences spur researchers on hunting for renewable, clean and low-cost energy alternatives [1–6]. Electrochemical water splitting is one of the hopeful ways to efficiently produce hydrogen with high purity, which is considered to be one of the most promising substitutes in the future [7–12]. However, as the other half reaction of water splitting, oxygen evolution reaction (OER) with the sluggish kinetics always dissipates excess energy and lowers the overall efficiency of the electrolysis, resulting in urgent need of high-performance electrocatalysts with low cost [13–18]. The well-accepted landmark OER electrocatalysts are noble metal oxides (such as RuO_2 and IrO_2), which are limited by their scarcity and consequently high cost [19–22]. So it still deserves researchers' great efforts to seek for high-performance OER electrocatalysts with earth-abundant non-noble elements.

It is known that Ni and Fe are abundant and geographically ubiquitous elements on the Earth [23–26], making NiFe-based compounds cheap and easily available, which is of great importance for OER electrocatalysts [27,28]. NiFe-based alloys and compounds are employed as high active OER electrocatalysts for decades, some of which are even superior to commercial noble metal oxides [29–31]. Exploring the origin of the high OER activity of NiFe-based compounds is never ending. Recent research has shown that pure NiOOH derived from bivalent Ni under anodic current is actually poor OER electrocatalysts [32,33]. It is the Fe impurity in the electrolyte (e.g., KOH) concentrated on that pure Ni-based electrocatalysts during electrolysis, the leads to the enhancement of both conductivity and OER activity [34]. NiFe-based electrocatalysts with inherent Fe have similar situation. The active ingredient for the enhanced OER performance is often thought to be Fe-doped NiOOH [35,36]. Additionally, the development of a facile

[1] Department of Chemistry, School of Science, and Tianjin Key Laboratory of Molecular Optoelectronic Science, Tianjin University, and Collaborative Innovation Center of Chemical Science and Engineering, Tianjin 300072, China.
[2] Analysis Center of Tianjin University, Tianjin University, Tianjin 300072, China
[†] These authors contributed equally to this work.
[*] Corresponding author (email: bzhang@tju.edu.cn)

method to prepare new efficient and inexpensive OER catalyst composed of earth-abundant Ni and Fe elements is highly desirable.

For electrochemical gas-generating reactions, self-supported electrodes with hydrophilic and aerophobic surface can always perform better electrocatalytic activity and stability. The hydrophility allows fast infiltration of electrolyte on the surface of the electrodes, which benefits the mass transport of the electrochemical reaction [37]. On the other hand, the aerophobicity of the electrodes means the generated bubbles on the surface can be easily desorbed, so that the working area will keep constant, and the electrocatalysts can reach a larger current density at the same applied overpotential [38]. In this sense, to fabricate electrocatalysts with super hydrophilic and aerophobic surface (such as nanosheet arrays and nanorod arrays) is of extreme importance for designing self-supported electrodes for electrochemical oxygen generation reaction.

Herein, we present, for the first time, the *in situ* formation of $NiFe_2O_4$-NiOOH nanosheet arrays supported on nickel foam (NF) (denoted as $NiFe_2O_4$-NiOOH) through a simple electrochemical anodization of crystalline Fe_2O_3 domains anchored on self-supported $Ni(OH)_2$ nanosheets on NF (denoted as Fe_2O_3-$Ni(OH)_2$) composite (Fig. 1a). *In situ* Raman spectroscopy indicates that $NiFe_2O_4$ formed during the first anodic scan can survive and play a vital role under rigorous OER conditions. The $NiFe_2O_4$-NiOOH possesses high OER activity to drive a current density of 30 mA cm^{-2} with a small overpotential of 240 mV. Surprisingly, the $NiFe_2O_4$-NiOOH can deliver an amazing current density of 3000 mA cm^{-2} with the overpotential of only 410 mV. This novel material is hoped to provide a new research model and can be instructive for investigating the intrinsic behaviors of the NiFe-based OER electrocatalysts.

EXPERIMENTAL SECTION

Synthesis of the $Ni(OH)_2$-Fe_2O_3/NF composite

NF was cut into rectangular shape of 1 cm × 3 cm. Before the reaction, NFs were immersed in acetone and 1 mol L^{-1} HCl for 15 min under sonication in sequence to remove the adsorbed organic molecules and oxide layer. Then the NFs were washed with deionized water and ethanol for three times, respectively, and dried in a vacuum oven for 6 h. For a typical synthesis, 0.32 g (0.8 mmol) $Fe(NO_3)_3{\cdot}9H_2O$ and 0.12 g (2 mmol) urea were dispersed in the mixture of 7 mL deionized water and 7 mL absolute ethanol under vigorous stirring in a 20 mL teflon-lined stainless-steel autoclave for about 30 min. A piece of freshly-treated NF was immersed into the mixture. Then the reactor was sealed, and treated at 120°C for 6 h. After the reactor cooled down naturally, the orange NF was picked out and washed several times with deionized water and ethanol, respectively. Then the product was dried in a vacuum oven for 6 h. The synthesis of $Ni(OH)_2$ nanosheets supported on NF and Fe_2O_3 nanoparticles had analogous procedures except for not adding $Fe(NO_3)_3{\cdot}9H_2O$ and NFs, respectively.

Characterization

The scanning electron microscopy (SEM) images were taken with a Hitachi S-4800 scanning electron microscope equipped with Thermo Scientific energy-dispersion X-ray fluorescence analyzer. Transmission electron microscopy (TEM), high resolution TEM (HRTEM) images, energy-dispersive X-ray (EDX) spectroscopic analysis and scanning transmission electron microscopy EDX (STEM-EDX) elemental distribution mapping were carried out with a JEM-2100F microscope. The X-ray diffraction (XRD) patterns were recorded with D8-Focus diffraction system with a Cu Kα source (λ = 1.54056 Å). Prior to the TEM and XRD measurements, several pieces of $Ni(OH)_2$-Fe_2O_3/NF were immersed in ethanol in a centrifugal tube, and were under ultrasonic continuously for more than 6 h. After that, the orange precipitate was isolated through centrifugation, dried in a vacuum oven for 6 h. X-ray photoelectron spectroscopy (XPS) was performed using Perkin Elmer PHI 1600 Versa Probe (Al Kα). All the peaks were calibrated with C 1s spectrum at binding energy of 284.8 eV. Raman spectroscopy was recorded on inVia reflex Raman microscope under an excitation of 532 nm laser light with power of 20 mW. The contact angle was measured in ambient condition on JC2000D optical contact angle measuring device by using nickel sheet instead of NF in the synthesis procedure.

Electrochemical measurements

All electrochemical measurements were performed by using an electrochemical workstation (CHI 660D, CH Instruments, Austin, TX) in a standard three-electrode system. 1.0 mol L^{-1} KOH was used as electrolyte for all electrochemical measurements, and degassed by bubbling oxygen for 30 min before the measurements. Glassy carbon rod electrode and Hg/HgO electrode with inner reference electrolyte of 1.0 mol L^{-1} KOH were used as counter and reference electrode, respectively. All the potentials referred in this paper were against reversible hydrogen electrode (RHE) without extra statement.

The scan rate for linear sweep voltammetry (LSV) curves

were 5 mV s^{-1}. The LSV curves were re-plotted as overpotential (η) *versus* log current density (log *j*/[*j*]) to get Tafel plots for quantification of the HER activities of the investigated catalysts. By fitting the linear portion of the Tafel plots to the Tafel equation ($\eta = b \log j/[j] + a$), the Tafel slope (*b*) was obtained. The cyclic voltammetry (CV) curves were swept between 0.6 and 0.8 V *vs.* Hg/HgO. And the *I*-*t* curves were measured at a constant potential of 0.65 V *vs.* Hg/HgO to get a current density of ~80 mA cm^{-2}. The electrochemical impedance spectroscopy spectra (EIS) were carried out at the potential of 0.65 V *vs.* Hg/HgO from 100,000 to 1 Hz at amplitude of 5 mV. Faradaic efficiency of the sample was measured with the assistance of water-gas displacing method by a burette at the potential of 0.7 V *vs.* Hg/HgO. The potentials mentioned in this paragraph were all without *iR* correction.

The as-prepared $Ni(OH)_2$-Fe_2O_3/NF was used as working electrode. Prior to the measurements, the $Ni(OH)_2$-Fe_2O_3/NF was carefully coated with epoxy, leaving exposed area of 0.5 cm^2. For powder samples (like RuO_2) drop-casted on NF as electrode, 2 mg catalyst powder was dispersed in 1 mL ethanol mixed with 20 μL 5 wt.% Nafion 117 solution, then the mixture was ultrasonicated for more than 30 min to acquire a homogeneous ink. Then 0.5 mL ink was carefully dropped uniformly on freshly treated bare NF with the same exposed area, and dried naturally.

In situ Raman spectroscopy

In situ Raman spectra were recorded on the aforementioned confocal Raman microscope under controlled potentials by the electrochemical workstation. The electrolytic cell was homemade by teflon with thin round quartz glass plate as cover to protect the objective. The self-supported working electrodes were inserted through the wall of the cell to keep the plane of working electrode perpendicular to the incident laser. Prior to the measurements, the working electrodes were carefully covered with epoxy and teflon tape to ensuring exposed area of 0.5 cm^2. A Pt wire as the counter electrode was rolled to a circle around the cell. Hg/HgO electrode with inner reference electrolyte of 1.0 mol L^{-1} KOH was used as the reference electrode. The accompanying applied potential of CV cycles was swept from 0 to 0.7 V *vs.* Hg/HgO in 0.05 mol L^{-1} KOH, ensuring that not too many bubbles would generate to block the light path.

RESULTS AND DISCUSSION

Precursor preparation and characterizations

As shown in Fig. 1a, Fe_2O_3-$Ni(OH)_2$ is prepared through a simple one-step reaction. Fig. 1b shows the panoramic SEM image of Fe_2O_3-$Ni(OH)_2$. The skeleton of the NF is well reserved, giving the possibility to directly use the as-obtained materials as working electrode. Upon closer SEM observation and TEM image, we can see vertical nanosheets with the layered size of hundreds to thousands nanometers and the thickness of ~9 nm distributed uniformly on the NF (Fig. 1c and Fig. S1 in Supplementary information). HRTEM image in Fig. 1d indicates the amorphous nature of the nanosheets with uniformly distributed crystalline domains (circled by yellow dotted line). The irregular-shape crystalline nanodomains show lattice fringes of 2.20 Å, which can be indexed to (113) interplanar spacing of α-Fe_2O_3. The selected area electron diffraction (SAED) pattern displays three bright circles, corresponding to (110), (202) and (300) planes of α-Fe_2O_3, respectively, indicating that the α-Fe_2O_3 domains are polycrystalline (inset in Fig. 1d). Moreover, the STEM-EDX elemental mapping shows that Fe, Ni and O are distributed uniformly throughout the whole nanosheet (Fig. 1e). And the corresponding EDX spectrum indicates the as-prepared sample is composed of Fe, Ni and O elements with no other impurities, and the molar ratio of Ni/Fe is about 4.6 (Fig. S2).

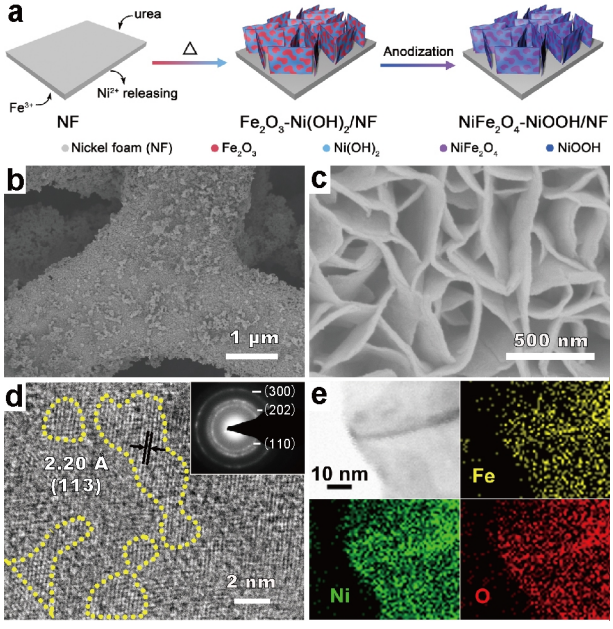

Figure 1 (a) Scheme illustrating the *in situ* transformation from Fe_2O_3-$Ni(OH)_2$ to $NiFe_2O_4$-NiOOH by a simple anodized treatment. (b) Low and (c) high magnification SEM images, (d) HRTEM image, (e) STEM-EDX elemental mapping of the as-prepared $Ni(OH)_2$-Fe_2O_3. The inset of (d) is the corresponding SAED pattern.

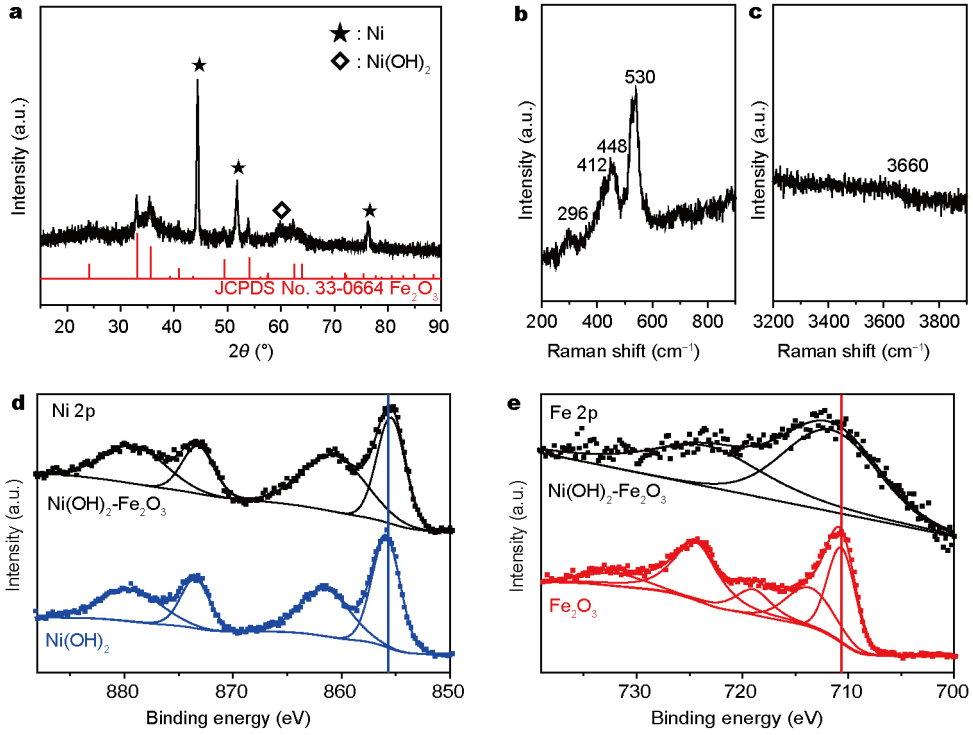

Figure 2 (a) XRD pattern and (b, c) Raman spectra of the as-prepared $Ni(OH)_2$-Fe_2O_3. (d) Ni 2p XPS spectra of $Ni(OH)_2$-Fe_2O_3 and $Ni(OH)_2$/NF nanosheets. (e) Fe 2p XPS spectra of the as-prepared $Ni(OH)_2$-Fe_2O_3 and Fe_2O_3 nanoparticles.

The typical XRD pattern of the Fe_2O_3-$Ni(OH)_2$ is shown in Fig. 2a. The peaks labeled by "★" correspond to metal nickel from NF, and the broad peak labeled by "◇" belongs to the poor crystalline $Ni(OH)_2$. Apart from the above peaks, all the rest peaks can be indexed to rhombohedral α-Fe_2O_3 (JCPDS No. 33-0664). To improve the crystallinity, the as-synthesized sample is calcined at 500°C in Ar. Obvious peaks assigned to NiO appear in the XRD pattern of the calcined sample as expected, confirming the existence of Ni oxy-compounds (Fig. S3). As a complement of XRD data, Raman spectroscopy is employed for further structural analysis. The bands at 296 and 412 cm^{-1} can be attributed to α-Fe_2O_3 (Fig. 2b) [39,40]. And the band locating at 448 cm^{-1} is assigned to Ni–O vibrations of α-$Ni(OH)_2$ and β-$Ni(OH)_2$, and the nearby 530 cm^{-1} band represents disordered structure of the $Ni(OH)_2$ (Fig. 2b) [35,41]. In the high wavenumber region of 3500–3700 cm^{-1}, which reflects the O–H bands of $Ni(OH)_2$, no obvious band but a broad corner appears at ~3660 cm^{-1}, implying that the as-prepared sample consists of disordered α-$Ni(OH)_2$ (Fig. 2c) [42]. The results of Raman analysis show that the as prepared-sample consists of α-Fe_2O_3 and disordered α-$Ni(OH)_2$, drawing a consistent conclusion with TEM and XRD, which indicates that the nanosheets of the as-prepared sample is composed of poor crystalline $Ni(OH)_2$ embedding with polycrystalline Fe_2O_3 nanoparticles.

XPS is used to depict the electronic structure of the Fe_2O_3-$Ni(OH)_2$. In Ni 2p spectra, the peaks at 855.5 and 873.1 eV can be attributed to Ni^{2+}. No obvious Ni^{3+} signal can be found (Fig. 2d) in Fe_2O_3-$Ni(OH)_2$ [43]. The binding energy peaks appeared in Fe 2p spectra at 724.8 and 712.0 eV belong to Fe^{3+} in α-Fe_2O_3 (Fig. 2e) [44]. XPS spectra of pure $Ni(OH)_2$ nanosheets on NF (shorted as $Ni(OH)_2$/NF) and Fe_2O_3 nanoparticles are also shown for comparison, both of which are synthesized through the similar routes (see details in SI, Figs S4–S7). Compared with Ni 2p spectra of pure $Ni(OH)_2$ nanosheets, the peaks of the as-prepared Fe_2O_3-$Ni(OH)_2$ show a negative shift of ~0.5 eV; while the corresponding Fe 2p spectra demonstrate the higher binding energy than pure Fe_2O_3 nanoparticles. The opposite peak shifts confirm the existence of electronic interaction between $Ni(OH)_2$ and Fe_2O_3 with an electron donation from Fe_2O_3 to $Ni(OH)_2$ in the as-synthesized Fe_2O_3-$Ni(OH)_2$ [45,46], implying that $Ni(OH)_2$ in Fe_2O_3-$Ni(OH)_2$ is more reductive and easy to be oxidized than the normal one.

Anodization and subsequent *ex situ* characterizations

Electrochemical transformation can be employed to pre-

pare materials which are difficult to synthesize by conventional approaches [47]. So the as-prepared Fe_2O_3-$Ni(OH)_2$ is anodized in a standard three-electrode system in 1.0 mol L^{-1} KOH by a simple anodic scan. After the anodization, the nanosheet structure, elemental content and distribution of the sample are almost unchanged (Figs S8, S9). However, HRTEM image of the anodized sample shows disordered lattice fringes, which is different from the precursor (Fig. 3a). In some tiny crystalline area, lattice fringes of 2.32 Å is assigned to (015) interplanar spacing of hydrated $Ni(OH)_2$ (JCPDS No. 38-0715). Additionally, great changes happen in *ex situ* Raman spectrum and XRD patterns.

As shown in Fig. 3b, all original Raman bands assigned to Fe_2O_3 and α-$Ni(OH)_2$ completely disappear, replacing by five new bands. The bands centered at 214, 332, 485 and 697 cm^{-1} could be undoubtedly attributed to $NiFe_2O_4$ [48]. However, the band at 564 cm^{-1} is uncertain to decide whether it belongs to $NiFe_2O_4$ or NiOOH. XRD pattern from the anodized sample is obtained for further structural analysis (Fig. 3c, bottom). Only broad peaks attributed to $Ni(OH)_2{\cdot}0.75H_2O$ (JCPDS No. 38-0715) can be found. To confirm the existence of possible $NiFe_2O_4$ affirmed by Raman spectroscopy, the post-OER sample is annealed at 500°C in high purity Ar for 4 h to improve the crystallinity. As expected, the newly-emerged peaks match well with the inverse spinel $NiFe_2O_4$ (JCPDS No. 86-2267, Fig. 3c, top). The peaks of NiO should be covered by $NiFe_2O_4$ because of the similar peak position. Note that $NiFe_2O_4$ cannot be observed for the thermal treatment of the as-prepared Fe_2O_3-$Ni(OH)_2$ (Fig. S3). It is reasonable to conjecture that amorphous $NiFe_2O_4$ can *in situ* form via the anodization process. No peaks assigned to Fe_2O_3 could be found, indicating the complete transformation of Fe_2O_3. It is unusual that the position and shape of peaks in Ni 2p XPS spectra of the anodized sample keep the same with those of the precursor, implying that electronic state of Ni does not change after the anodization (Fig. 3d). Since CV cycles can lead to periodic change of the structure, samples are chosen undergoing more than 20 times anodic forward scan without backward. And two individual anodized samples were measured to ensure accuracy. The cross-check result indicates that no NiOOH is detected in *ex situ* XPS.

In situ Raman spectroscopic analysis of transformation mechanism

Since NiOOH is thermodynamically unstable [49], *in situ* Raman spectroscopy is employed to monitor the transfor-

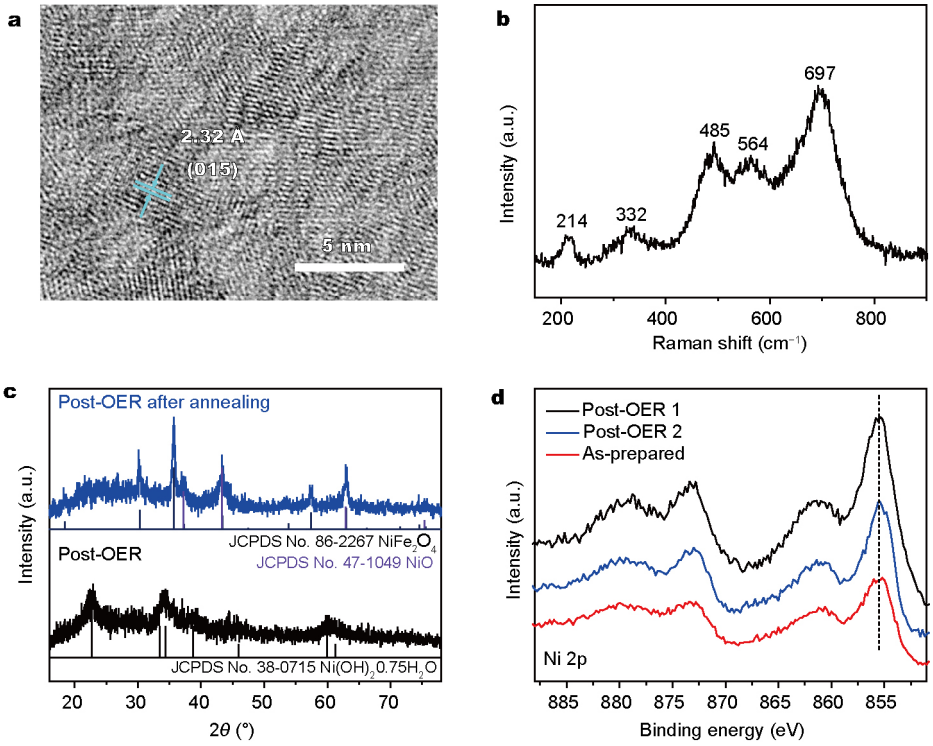

Figure 3 (a) HRTEM image, (b) Raman spectrum, (c) XRD patterns and (d) Ni 2p XPS spectra of the anodized sample. To ensure accuracy, two individual anodized samples were measured in (d) for XPS analysis.

mation during anodization [50]. In the anodization process, it is found that the first anodic scan shows remarkable difference compared with the subsequent scans (Fig. 4a). So we choose the first two cycles to carry out the *in situ* Raman spectroscopy. The initial Raman spectrum is nearly the same to that of the precursor in Fig. 2b, except for the weakened signal intensity probably due to the laser scatting by the quartz glass and electrolyte on the light path (Fig. 4b). As shown in Fig. 4c, with the applied potential increasing from 0 to 0.6 V *vs.* Hg/HgO, the band intensity of 475 and 558 cm^{-1} increases gradually as well, which indicates the formation of NiOOH under growing anodic potential. At the potential of 0.4 V *vs.* Hg/HgO, a characteristic band centered at ~700 cm^{-1} comes into being, implying the beginning formation of $NiFe_2O_4$ (inset in Fig. 4c). In the following backward scan, the bands attributed to NiOOH fade away with the potential decreasing, just as the *in situ* Raman spectra of $Ni(OH)_2$ (Fig. S10). In contrast, the intensity of band at 700 cm^{-1} is gradually enhanced at the same time (Fig. 4d). When the potential back to 0 V *vs.* Hg/HgO, the bands of 330, 487 and 698 cm^{-1} can be unambiguously ascribed to $NiFe_2O_4$, while the band at 527 cm^{-1} belongs to the residual $Ni(OH)_2$. No band assigned to NiOOH is left at this point (Fig. 4e).

During the second cycle, the bands corresponding to NiOOH show periodic appearance and disappearance just as the first cycle. In the meantime, the intensity of the characteristic band of $NiFe_2O_4$ at ~700 cm^{-1} remains un-

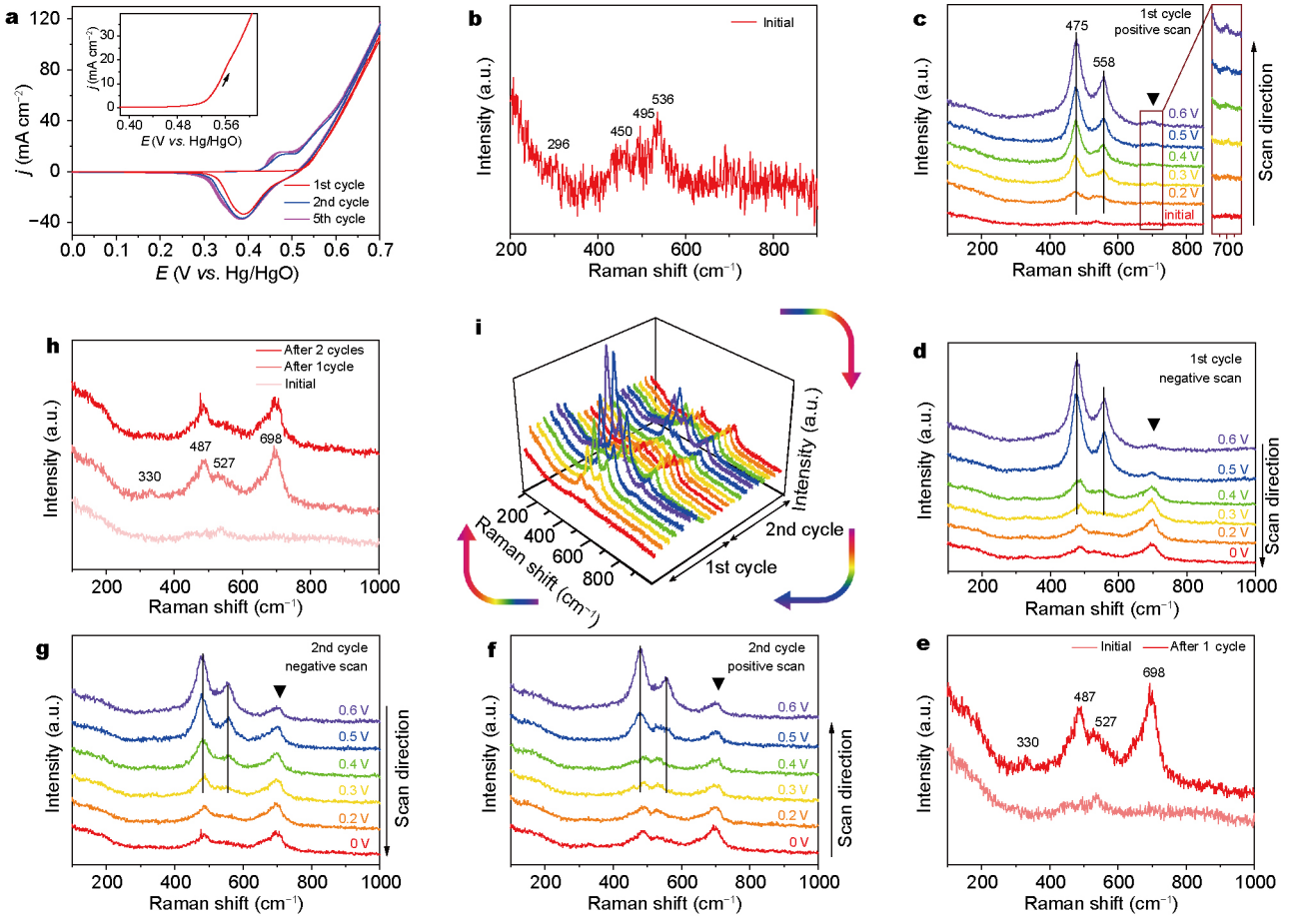

Figure 4 Anodization and accompanying *in situ* potential-dependent Raman spectra. (a) The first five CVs of the as-prepared sample without *iR* compensation in 1.0 mol L^{-1} KOH. The inset of (a) is the magnification of positive scan in first cycle. (b–e) Raman spectra acquired at different potentials in the first CV cycle. (b) Initial Raman spectrum without any applied potential. (c, d) Raman spectra at different potentials in forward (c) and backward (d) anodic scan in the 1st CV cycle. The inset of (c) is the magnification of the spectra at ~700 cm^{-1} Raman shift. (e) Comparison of Raman spectra before and after 1st cycle. (f–h) Raman spectra at different potentials in the 2nd CV cycle. (f, g) Raman spectra at different potentials in forward (f) and backward (g) anodic scan in the 2nd CV cycle. (h) Comparison of Raman spectra before and after every cycle. (i) Three-dimensional Raman spectra acquired at different potentials for all the two cycles. All the potentials referred in this figure are against Hg/HgO. The black lines in (c), (d), (f), and (g) represent the band position of NiOOH. The bands at ~700 cm^{-1} labeled by "▼" correspond to $NiFe_2O_4$.

changed throughout this cycle (Fig. 4f, g). When the potential is back to 0 *vs.* Hg/HgO again, nearly no difference can be found between these two recursive spectra (Fig. 4h). The three-dimensional potential-dependent Raman spectra of the two cycles can give a comprehensive and visual tendency of the transformation (Fig. 4i). Band intensity of NiOOH strictly follows periodical change of the potential, while $NiFe_2O_4$ gradually forms in the first CV cycle and can stay the same for the rest time. The stability of $NiFe_2O_4$ can be confirmed by potential-dependent *in situ* Raman spectra of the same sample after 500 CV cycles (Fig. S11). The result shows that $NiFe_2O_4$ can maintain its intensity even after long-time OER CV cycles.

It can be found that the formation of NiOOH in the first scan is around 0.2 V *vs.* Hg/HgO (Fig. 4c), which is not only much earlier than many previous reports (around 0.4–0.5 V) [35,51], but also even earlier than that in the 2nd and 500th cycles (Fig. 4f and Fig. S11). Note that the beginning formation of $NiFe_2O_4$ is ~0.3 V *vs.* Hg/HgO and no obvious peak appears in this region in the first positive scan curve (inset in Fig. 4a). We assume that $NiFe_2O_4$ is transformed from newly formed NiOOH and the surrounding Fe_2O_3 on the premise of the strong electronic interaction between Fe_2O_3 and $Ni(OH)_2$, as confirmed by XPS spectra (see more discussion in Fig. S12 in SI). The electron donation from Fe_2O_3 to $Ni(OH)_2$ makes the electron density of $Ni(OH)_2$ a little larger than the normal, resulting in the easier oxidation of $Ni(OH)_2$ to NiOOH at relatively low anodic potential and easier reaction between the newly formed NiOOH and Fe_2O_3. Only dropcasting Fe_2O_3 nanoparticles onto $Ni(OH)_2$/NF cannot lead to an easier oxidation of $Ni(OH)_2$ and the following transformation of $NiFe_2O_4$ (Figs S10, S11) due to the lack of interaction. It is worth mentioning that thermodynamically unstable NiOOH will spontaneously degrade to $Ni(OH)_2$ during the period of waiting for *ex situ* measurements, making *in situ* Raman spectroscopy extremely important to shed light on the transformation mechanism of our sample. Moreover, our findings could also provide a mild room-temperature electrochemical strategy to synthesize amorphous spinel materials which should be usually synthesized by extremely high temperature calcination (e.g., over 800°C).

OER activity evaluations at steady state

The OER activities of the sample were measured in 1.0 mol L^{-1} KOH in a standard three-electrode system as well. And the self-supported $NiFe_2O_4$-NiOOH was used as working electrode directly. The LSV curves and the corresponding Tafel slopes of different samples are shown in Fig. 5a, b. As a benchmark, the OER activity of commercial RuO_2 supported on NF was first examined. And the commercial RuO_2 shows an excellent OER activity of a low overpotential of 275 mV to reach current density of 30 mA cm^{-2}. However, the $NiFe_2O_4$-NiOOH only needs an overpotential of 240 mV to reach the same current density of 30 mA cm^{-2}, which is not only better than RuO_2, but also exceeds many other reported NiFe-based compounds (Table S1). In addition, with the anodic potential increasing, the $NiFe_2O_4$-NiOOH can acquire current density of 100 mA cm^{-2} with the overpotential of 270 mV. Moreover, it only needs the overpotential of ~410 mV to achieve an amazing current density of as large as 3000 mA cm^{-2} (inset in Fig. 5a). Moreover, the $NiFe_2O_4$-NiOOH performs a small Tafel slope of 55 mV dec^{-1}, smaller than the value of commercial RuO_2 of 58 mV dec^{-1} (Fig. 5b). As comparison, LSV curves of pure $Ni(OH)_2$ nanosheets and Fe_2O_3 nanoparticles on $Ni(OH)_2$/NF synthesized through the same method are also examined. Both of them perform poor OER activity as expected. After 1000 CV cycles, LSV curves of the $NiFe_2O_4$-NiOOH can almost overlap with the initial one (Fig. 5c). Also, the $NiFe_2O_4$-NiOOH can maintain the current density of ~80 mA cm^{-2} for more than 100 h (inset in Fig. 5c). In addition, the $NiFe_2O_4$-NiOOH also shows a small charge transfer resistance in Nyquist plots and a high Faradaic efficiency of ~100 % (Fig. 5d and Figs S13, S14). All the above results reveal that the as-prepared $NiFe_2O_4$-NiOOH is adequate for OER with high activity and high stability.

The synergistic effect of NiOOH and amorphous $NiFe_2O_4$ is thought to make main contribution to the excellent OER performance. Recently, $NiFe_2O_4$ is reported to be possible OER active species [52]. Li and Selloni [53] have demonstrated theoretically that $NiFe_2O_4$ (001) surface owns excellent OER activity, which is even better than some kind of Fe-doped NiOOH. These reports provide powerful evidence for us to confirm the significance of $NiFe_2O_4$ for oxygen evolution. Fe-doped NiOOH is a well-studied OER active intermediate in both practice and theoretical calculation. However, limited by our testing techniques, it is difficult to estimate if NiOOH in our material is doped by Fe or not. So we attribute the high OER activity to the integration of NiOOH and $NiFe_2O_4$. Without the assistance of $NiFe_2O_4$, only $Ni(OH)_2$/NF does not perform very well in this situation. The amorphism of $NiFe_2O_4$ also shows an important influence on the OER activity. The OER performance can be greatly impaired after the annealing of $NiFe_2O_4$-NiOOH at high temperature to reinforce the crystallinity (Fig. S15).

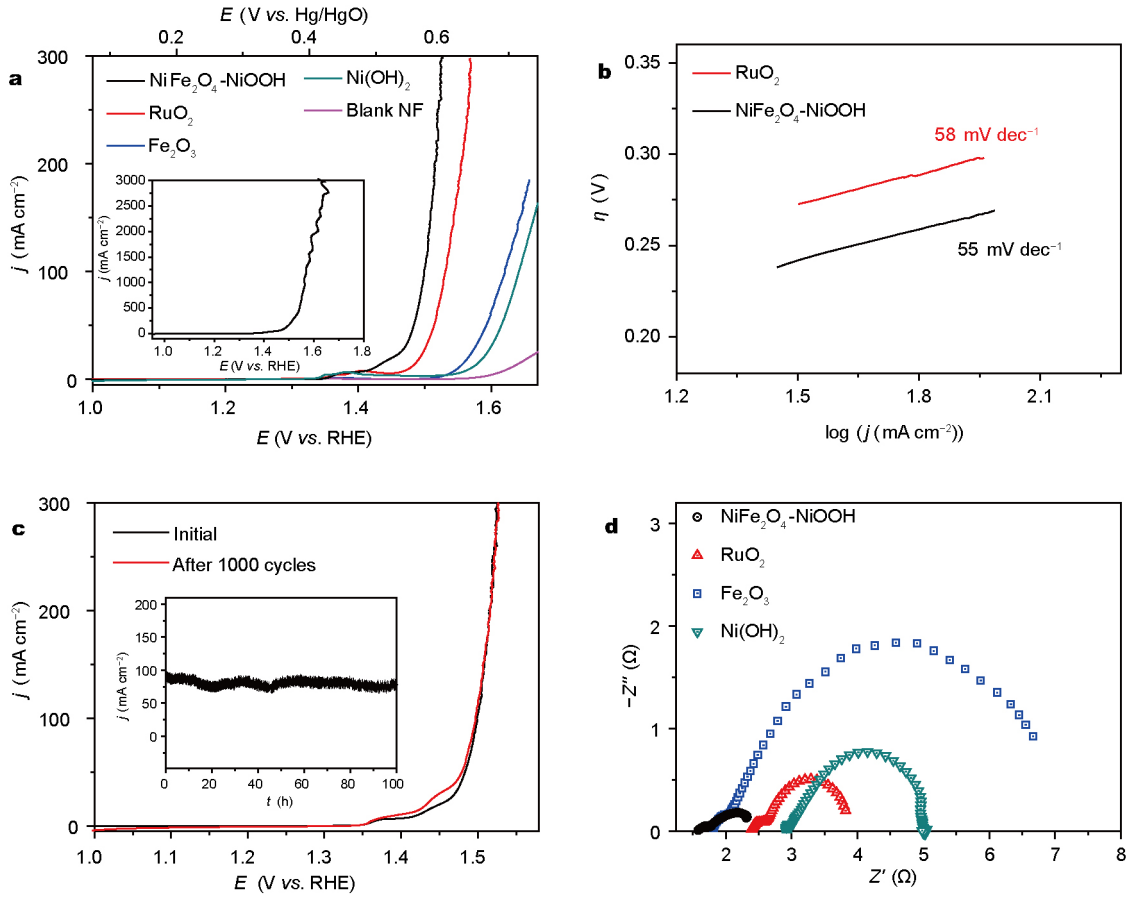

Figure 5 (a) LSV curves of $NiFe_2O_4$-NiOOH, RuO_2, Fe_2O_3, $Ni(OH)_2$ and blank NF with *iR* correction. The inset of (a) is the whole LSV curve of $NiFe_2O_4$-NiOOH. (b) *iR* corrected Tafel slopes of $NiFe_2O_4$-NiOOH and RuO_2. (c) *iR* corrected LSV curves before and after 1000 CV cycles for oxygen generation of $NiFe_2O_4$-NiOOH. The inset of (c) is *j*-*t* curve of $NiFe_2O_4$-NiOOH. (d) Nyquist plots of $NiFe_2O_4$-NiOOH, RuO_2, Fe_2O_3, and $Ni(OH)_2$.

The remarkable OER performance can be partly attributed to the hydrophilic and aerophobic surface formed by the nanosheet array structure. When water is dropped on the surface of $NiFe_2O_4$-NiOOH, it will spread out completely at once, exhibiting super hydrophility of the sample, which benefits the mass transport of the reaction thus improving the activity of $NiFe_2O_4$-NiOOH (Fig. 6a and Video S1). Additionally, it can be observed that the generated gas bubbles can release more easily from the surface of the $NiFe_2O_4$-NiOOH than from the dropcasting one so that a constant working area is kept, which is helpful to acquire steady and large current density during electrochemical measurements, showing the aerophobic surface of the $NiFe_2O_4$-NiOOH (Fig. 6b, c). Both the aerophobicity and hydrophility avail the OER by promoting the OER activity and stability of $NiFe_2O_4$-NiOOH and allowing a huge current density. It is worth noting that the underneath NF substrate also makes contribution to the enhanced OER performance by facilitating mass transport and improving

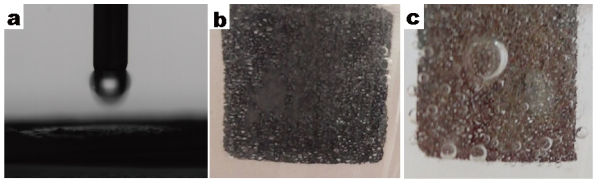

Figure 6 (a) Contact angle measurement of $NiFe_2O_4$-NiOOH. (b, c) Optical photos of (b) $NiFe_2O_4$-NiOOH and (c) Fe_2O_3 drop-casted on NF during electrochemical oxygen evolution.

the conductivity of $NiFe_2O_4$-NiOOH [54–57]. All these features make $Ni(OH)_2$-Fe_2O_3 a competent OER electrocatalyst with high activity and high stability.

CONCLUSIONS

In summary, self-supported $NiFe_2O_4$-NiOOH is fabricated through a simple anodization of Fe_2O_3-$Ni(OH)_2$. The as-prepared Fe_2O_3-$Ni(OH)_2$ shows strong electronic interaction with the electron donation of Fe_2O_3 to $Ni(OH)_2$,

making $Ni(OH)_2$ much more easily to be oxidized to NiOOH. The results of *in situ* Raman spectra indicate that newly-formed NiOOH together with surrounding Fe_2O_3 is tend to electrochemically *in situ* transform into amorphous $NiFe_2O_4$ in the first anodic scan. The $NiFe_2O_4$-NiOOH can deliver the current density of 30 mA cm^{-2} with a small overpotential of 240 mV, and only requires the overpotential of 410 mV to achieve an amazing huge current density of 3000 mA cm^{-2}. The excellent OER performance can be attributed to the integration of amorphous $NiFe_2O_4$ and NiOOH. The *in situ* transformation strategy should be a new addition to the conversion chemistry of nanomaterials [58–60], and may be a reminder to people for the possible electrochemical transformation in composite materials. Additionally, our findings will not only provide an instructive example for investigating the intrinsic behaviours of the NiFe-based OER electrocatalysts, but also point out a mild method to synthesize amorphous spinel materials at room temperature.

Received 17 February 2017; accepted 3 March 2017; published online 16 March 2017

1 Lewis NS, Nocera DG. Powering the planet: chemical challenges in solar energy utilization. Proc Natl Acad Sci USA, 2006, 103: 15729–15735
2 Faber MS, Jin S. Earth-abundant inorganic electrocatalysts and their nanostructures for energy conversion applications. Energ Environ Sci, 2014, 7: 3519–3542
3 Hunter BM, Gray HB, Müller AM. Earth-abundant heterogeneous water oxidation catalysts. Chem Rev, 2016, 116: 14120–14136
4 Zhang B, Zheng X, Voznyy O, *et al.* Homogeneously dispersed multimetal oxygen-evolving catalysts. Science, 2016, 352: 333–337
5 Jiao Y, Zheng Y, Davey K, *et al.* Activity origin and catalyst design principles for electrocatalytic hydrogen evolution on heteroatom-doped graphene. Nat Energ, 2016, 1: 16130
6 Lu S, Zhuang Z. Electrocatalysts for hydrogen oxidation and evolution reactions. Sci China Mater, 2016, 59: 217–238
7 Wang HY, Hung SF, Chen HY, *et al.* *In operando* identification of geometrical-site-dependent water oxidation activity of spinel Co_3O_4. J Am Chem Soc, 2016, 138: 36–39
8 Xu L, Jiang Q, Xiao Z, *et al.* Plasma-engraved Co_3O_4 nanosheets with oxygen vacancies and high surface area for the oxygen evolution reaction. Angew Chem Int Ed, 2016, 55: 5277–5281
9 Xia BY, Yan Y, Li N, *et al.* A metal–organic framework-derived bifunctional oxygen electrocatalyst. Nat Energ, 2016, 1: 15006
10 Chen W, Liu Y, Li Y, *et al.* *In situ* electrochemically derived nanoporous oxides from transition metal dichalcogenides for active oxygen evolution catalysts. Nano Lett, 2016, 16: 7588–7596
11 Yin J, Zhou P, An L, *et al.* Self-supported nanoporous $NiCo_2O_4$ nanowires with cobalt–nickel layered oxide nanosheets for overall water splitting. Nanoscale, 2016, 8: 1390–1400
12 Zeng M, Wang H, Zhao C, *et al.* 3D graphene foam-supported cobalt phosphate and borate electrocatalysts for high-efficiency water oxidation. Sci Bull, 2015, 60: 1426–1433
13 Ng JWD, García-Melchor M, Bajdich M, *et al.* Gold-supported cerium-doped NiO_x catalysts for water oxidation. Nat Energ, 2016, 1: 16053
14 Lu X, Zhao C. Electrodeposition of hierarchically structured three-dimensional nickel–iron electrodes for efficient oxygen evolution at high current densities. Nat Commun, 2015, 6: 6616
15 Xu X, Song F, Hu X. A nickel iron diselenide-derived efficient oxygen-evolution catalyst. Nat Commun, 2016, 7: 12324
16 Fan K, Chen H, Ji Y, *et al.* Nickel–vanadium monolayer double hydroxide for efficient electrochemical water oxidation. Nat Commun, 2016, 7: 11981
17 Feng JX, Ye SH, Xu H, *et al.* Design and synthesis of FeOOH/CeO_2 heterolayered nanotube electrocatalysts for the oxygen evolution reaction. Adv Mater, 2016, 28: 4698–4703
18 Chen Z, Zhao H, Zhang J, *et al.* IrNi nanoparticle-decorated flower-shaped $NiCo_2O_4$ nanostructures: controllable synthesis and enhanced electrochemical activity for oxygen evolution reaction. Sci China Mater, 2017, 60: 119–130
19 Chen P, Xu K, Fang Z, *et al.* Metallic Co_4N porous nanowire arrays activated by surface oxidation as electrocatalysts for the oxygen evolution reaction. Angew Chem Int Ed, 2015, 54: 14710–14714
20 Zhao Y, Jia X, Chen G, *et al.* Ultrafine NiO nanosheets stabilized by TiO_2 from monolayer NiTi-LDH precursors: an active water oxidation electrocatalyst. J Am Chem Soc, 2016, 138: 6517–6524
21 Wu J, Ren Z, Du S, *et al.* A highly active oxygen evolution electrocatalyst: ultrathin CoNi double hydroxide/CoO nanosheets synthesized via interface-directed assembly. Nano Res, 2016, 9: 713–725
22 Du S, Ren Z, Zhang J, *et al.* Co_3O_4 nanocrystal ink printed on carbon fiber paper as a large-area electrode for electrochemical water splitting. Chem Commun, 2015, 51: 8066–8069
23 Gopalaiah K. Chiral iron catalysts for asymmetric synthesis. Chem Rev, 2013, 113: 3248–3296
24 Izatt RM, Izatt SR, Bruening RL, *et al.* Challenges to achievement of metal sustainability in our high-tech society. Chem Soc Rev, 2014, 43: 2451–2475
25 Jia X, Zhao Y, Chen G, *et al.* Ni_3FeN nanoparticles derived from ultrathin NiFe-layered double hydroxide nanosheets: an efficient overall water splitting electrocatalyst. Adv Energ Mater, 2016, 6: 1502585
26 Fan H, Huang X, Shang L, *et al.* Controllable synthesis of ultrathin transition-metal hydroxide nanosheets and their extended composite nanostructures for enhanced catalytic activity in the heck reaction. Angew Chem Int Ed, 2016, 55: 2167–2170
27 Feng LL, Yu G, Wu Y, *et al.* High-index faceted Ni_3S_2 nanosheet arrays as highly active and ultrastable electrocatalysts for water splitting. J Am Chem Soc, 2015, 137: 14023–14026
28 Ni B, Wang X. Edge overgrowth of spiral bimetallic hydroxides ultrathin-nanosheets for water oxidation. Chem Sci, 2015, 6: 3572–3576
29 Gong M, Li Y, Wang H, *et al.* An advanced Ni–Fe layered double hydroxide electrocatalyst for water oxidation. J Am Chem Soc, 2013, 135: 8452–8455
30 Qian L, Lu Z, Xu T, *et al.* Trinary layered double hydroxides as high-performance bifunctional materials for oxygen electrocatalysis. Adv Energ Mater, 2015, 5: 1500245
31 Li Z, Shao M, An H, *et al.* Fast electrosynthesis of Fe-containing layered double hydroxide arrays toward highly efficient electrocatalytic oxidation reactions. Chem Sci, 2015, 6: 6624–6631
32 Görlin M, Chernev P, Ferreira de Araújo J, *et al.* Oxygen evolution reaction dynamics, faradaic charge efficiency, and the active metal redox states of Ni–Fe oxide water splitting electrocatalysts. J Am Chem Soc, 2016, 138: 5603–5614

33 Friebel D, Louie MW, Bajdich M, *et al.* Identification of highly active Fe sites in (Ni,Fe)OOH for electrocatalytic water splitting. J Am Chem Soc, 2015, 137: 1305–1313
34 Burke MS, Enman LJ, Batchellor AS, *et al.* Oxygen evolution reaction electrocatalysis on transition metal oxides and (oxy)hydroxides: activity trends and design principles. Chem Mater, 2015, 27: 7549–7558
35 Louie MW, Bell AT. An investigation of thin-film Ni–Fe oxide catalysts for the electrochemical evolution of oxygen. J Am Chem Soc, 2013, 135: 12329–12337
36 Trotochaud L, Young SL, Ranney JK, *et al.* Nickel–iron oxyhydroxide oxygen-evolution electrocatalysts: the role of intentional and incidental iron incorporation. J Am Chem Soc, 2014, 136: 6744–6753
37 Li Y, Zhang H, Xu T, *et al.* Under-water superaerophobic pine-shaped Pt nanoarray electrode for ultrahigh-performance hydrogen evolution. Adv Funct Mater, 2015, 25: 1737–1744
38 Shi Y, Zhang B. Recent advances in transition metal phosphide nanomaterials: synthesis and applications in hydrogen evolution reaction. Chem Soc Rev, 2016, 45: 1529–1541
39 Tian W, Wang X, Zhi C, *et al.* $Ni(OH)_2$ nanosheet @ Fe_2O_3 nanowire hybrid composite arrays for high-performance supercapacitor electrodes. Nano Energ, 2013, 2: 754–763
40 Ahmmad B, Leonard K, Shariful Islam M, *et al.* Green synthesis of mesoporous hematite (α-Fe_2O_3) nanoparticles and their photocatalytic activity. Adv Powder Tech, 2013, 24: 160–167
41 Vidotti M, Salvador RP, Córdoba de Torresi SI. Synthesis and characterization of stable Co and Cd doped nickel hydroxide nanoparticles for electrochemical applications. Ultrason Sonochem, 2009, 16: 35–40
42 Bernard MC, Bernard P, Keddam M, *et al.* Characterisation of new nickel hydroxides during the transformation of α $Ni(OH)_2$ to β $Ni(OH)_2$ by ageing. Electrochim Acta, 1996, 41: 91–93
43 Li X, Han GQ, Liu YR, *et al.* *In situ* grown pyramid structures of nickel diselenides dependent on oxidized nickel foam as efficient electrocatalyst for oxygen evolution reaction. Electrochim Acta, 2016, 205: 77–84
44 Hu X, Yu JC, Gong J, *et al.* α-Fe_2O_3 nanorings prepared by a microwave-assisted hydrothermal process and their sensing properties. Adv Mater, 2007, 19: 2324–2329
45 Xu YF, Gao MR, Zheng YR, *et al.* Nickel/nickel(II) oxide nanoparticles anchored onto cobalt(IV) diselenide nanobelts for the electrochemical production of hydrogen. Angew Chem Int Ed, 2013, 52: 8546–8550
46 Gao MR, Xu YF, Jiang J, *et al.* Water oxidation electrocatalyzed by an efficient Mn_3O_4/$CoSe_2$ nanocomposite. J Am Chem Soc, 2012, 134: 2930–2933
47 Fray DJ, Chen GZ, Farthing TW. Direct electrochemical reduction of titanium dioxide to titanium in molten calcium chloride. Nature, 2000, 407: 361–364
48 Ahlawat A, Sathe VG. Raman study of $NiFe_2O_4$ nanoparticles, bulk and films: effect of laser power. J Raman Spectrosc, 2011, 42: 1087–1094
49 Melendres CA. *In situ* laser raman spectroscopic study of anodic corrosion films on nickel and cobalt. J Electrochem Soc, 1984, 131: 2239–2243
50 Li CY, Dong JC, Jin X, *et al.* *In situ* monitoring of electrooxidation processes at gold single crystal surfaces using shell-isolated nanoparticle-enhanced raman spectroscopy. J Am Chem Soc, 2015, 137: 7648–7651
51 Yeo BS, Bell AT. *In situ* raman study of nickel oxide and gold-supported nickel oxide catalysts for the electrochemical evolution of oxygen. J Phys Chem C, 2012, 116: 8394–8400
52 Landon J, Demeter E, İnoğlu N, *et al.* Spectroscopic characterization of mixed Fe–Ni oxide electrocatalysts for the oxygen evolution reaction in alkaline electrolytes. ACS Catal, 2012, 2: 1793–1801
53 Li YF, Selloni A. Mechanism and activity of water oxidation on selected surfaces of pure and Fe-doped NiO_x. ACS Catal, 2014, 4: 1148–1153
54 Long X, Li J, Xiao S, *et al.* A strongly coupled graphene and FeNi double hydroxide hybrid as an excellent electrocatalyst for the oxygen evolution reaction. Angew Chem Int Ed, 2014, 53: 7584–7588
55 Wang H, Lee HW, Deng Y, *et al.* Bifunctional non-noble metal oxide nanoparticle electrocatalysts through lithium-induced conversion for overall water splitting. Nat Commun, 2015, 6: 7261
56 Ping J, Wang Y, Lu Q, *et al.* Self-assembly of single-layer CoAl-layered double hydroxide nanosheets on 3D graphene network used as highly efficient electrocatalyst for oxygen evolution reaction. Adv Mater, 2016, 28: 7640–7645
57 Wang J, Li K, Zhong H, *et al.* Synergistic effect between metal-nitrogen-carbon sheets and NiO nanoparticles for enhanced electrochemical water-oxidation performance. Angew Chem Int Ed, 2015, 54: 10530–10534
58 Wang H, Zhuo S, Liang Y, *et al.* General self-template synthesis of transition-metal oxide and chalcogenide mesoporous nanotubes with enhanced electrochemical performances. Angew Chem Int Ed, 2016, 55: 9055–9059
59 Ye X, Jones MR, Frechette LB, *et al.* Single-particle mapping of nonequilibrium nanocrystal transformations. Science, 2016, 354: 874–877
60 Li K, Zhang J, Wu R, *et al.* Anchoring CoO domains on $CoSe_2$ nanobelts as bifunctional electrocatalysts for overall water splitting in neutral media. Adv Sci, 2016, 3: 1500426

Acknowledgments This work was supported by the National Natural Science Foundation of China (21422104) and the Key Project of Natural Science Foundation of Tianjin City (16JCZDJC30600). We acknowledge Prof. Bin Ren for kind discussion.

Author contributions Zhang B conceived and directed the project. Zhang B, Zhang F and Shi Y designed the experiments. Zhang F and Shi Y carried out the experiments. Shi Y, Zhang J and Zhang B analyzed the data. Shi Y, Xue T and Liang Y performed the *in situ* Raman spectroscopic measurements. Shi Y and Zhang B wrote the paper. All authors discussed the results and commented on the paper.

Conflict of interest The authors declare that they have no conflict of interest.

Supplementary information Additional characterizations, Raman spectra and electrochemical measurments are available in the online version of this paper.

Fang Zhang is currently a Master candidate at Tianjin University under the supervision of Prof. Bin Zhang. She received her BSc degree from the College of Chemistry, Chemical Engineering and Materials Science from Shandong Normal University in 2014. Her research interests include the development of non-noble metal electrocatalysts for oxygen evolution reaction.

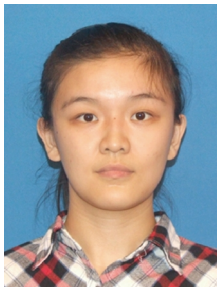

Yanmei Shi received her BSc degree in applied chemistry from Tianjin University in 2013. She is currently working for her PhD degree at Tianjin University under the supervision of Prof. Bin Zhang. Her research focuses on the development of non-noble metal electrocatalysts for hydrogen and oxygen evolution reactions.

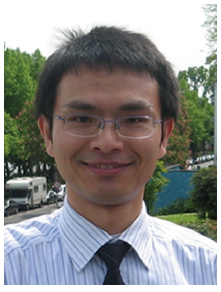

Bin Zhang received his PhD degree from the University of Science and Technology of China in 2007. He carried out postdoctoral research in the University of Pennsylvania (2007.7–2008.7) and worked as an Alexander von Humboldt fellow in Max Planck Institute of Colloids and Interfaces (2008.8–2009.7). Currently, he is a professor in the Chemistry Department at Tianjin University and Collaborative Innovation Center of Chemical Science and Engineering (Tianjin). His research mainly focuses on the development of chemical transformation strategy to prepare porous and ultrathin nanomaterials, and their hybrids for energy catalytic applications.

Fe_2O_3-$Ni(OH)_2$原位电化学转化为$NiFe_2O_4$-NiOOH用于高效电解水产氧

张芳[1†], 史艳梅[1†], 薛涛[2], 张競方[1], 梁瑜[1], 张兵[1*]

摘要 探索新的催化活性物种和开发价格低廉、来源广泛的镍铁基电催化剂对实现高效电解水产氧有着重要意义. 本文报道了一种通过阳极化镶嵌Fe_2O_3颗粒的$Ni(OH)_2$纳米片阵列, 使其原位电化学转化成$NiFe_2O_4$-NiOOH纳米片阵列用于高效电解水产氧的复合催化剂. 电化学产氧测试表明: 这种复合材料催化剂在电流密度达到30 mA cm^{-2}时仅需240 mV的过电势, 且只需要410 mV的过电势就可使电流密度达到3000 mA cm^{-2}. 电化学原位拉曼光谱测试表明: 这种镶嵌有Fe_2O_3颗粒的$Ni(OH)_2$纳米片中的$Ni(OH)_2$拥有更高的反应活性, 从而使其不仅更容易氧化生成NiOOH, 同时新生成的NiOOH可以在正电流的刺激下与Fe_2O_3颗粒反应原位生成非晶的$NiFe_2O_4$-NiOOH复合材料. 该复合材料的高电化学产氧活性主要归因于$NiFe_2O_4$和NiOOH的协同作用, 以及由于纳米片阵列结构所导致的超疏气与超亲水表面. 这项工作不仅从全新的角度解读了镍铁基催化剂高电催化产氧活性的起源, 同时还提供了一种温和的室温合成方法用以制备具有非晶结构的尖晶石类材料. 此外, 该项工作还有助于研究者关注异质催化剂在电催化过程中的物质转化行为, 从而更好地设计和发展新型高效催化体系.